Effects of Pb^{2+} doping on $La_4Ti_9O_{24}$ ceramics

Yuan-Wen Liu · Pang Lin · Ming-Wen Chu

Abstract The kinetic structural evolution of the Pb^{2+}-doped $La_4Ti_9O_{24}$ ceramics was investigated. Using electron diffraction and Rietveld analysis of the X-ray powder diffraction patterns, we show that the increase in Pb^{2+} doping results in the structural transition from $La_4Ti_9O_{24}$ to a $La_{2/3}TiO_3$-type phase (*Ibmm*, No. 74). Further kinetic studies of Pb^{2+} diffusion into $La_4Ti_9O_{24}$ ceramics suggest that the $La_4Ti_9O_{24}$–$La_{2/3}TiO_3$ phase transition requires an activation energy of 607 ± 60 kJ/mol.

Introduction

The La_2O_3–TiO_2 system exhibits interesting dielectric properties. In the study of MacChesney et al. [1], there exists three dielectric binary compounds, $La_4Ti_9O_{24}$, $La_2Ti_2O_7$, and La_2TiO_5, in this class. More recently, Ška-pin et al. [2] suggested that the two new phases, $La_4Ti_3O_{12}$ and $La_{2/3}TiO_3$, should be incorporated into this material system.

The crystal structure of $La_4Ti_9O_{24}$ has been resolved by Morris et al. [3] using the orthorhombic space group *Fddd* (No. 70) with the lattice parameters $a = 1.41458(1)$ nm, $b = 3.55267(4)$ nm, and $c = 1.45794(1)$ nm. The $La_4Ti_9O_{24}$

lattice consists of a complex network of distorted titanium octahedra, showing corner- and edge-shared characteristics with one 8-fold and two crystallographically distinct 6-fold lanthanum ions in the structure. Figure 1a shows the unit cell of $La_4Ti_9O_{24}$ in [001] direction. The La(3)-centered polyhedra form flat layers parallel to the *ac* plane (see the arrows in Fig. 1a), and the sandwiched region between two consecutive La(3)-centered polyhedra is composed of distorted TiO_6 octahedra that exhibit corner- and edge-shared features (see Fig. 1b, c). Furthermore, $Ti(3)O_6$ shows less distorted characteristics compared to the other four crystallographically distinct TiO_6 octahedra [3]. In a separate work [4], $La_4Ti_9O_{24}$ was reported to possess good microwave dielectric properties, the relative dielectric constant (ϵ_r) ~37, the quality factor (Q) ~3060 at 8.1 GHz, and the temperature coefficient of the resonant frequency (TCF) ~15 ppm/°C.

The $La_{2/3}TiO_3$-type perovskite recently attracts significant attention due to its remarkable optical [5, 6], electrical [7–12], and microwave dielectric properties [13–18]. The structure of this A-site deficient phase is, however, unstable considering the associated high vacancy concentration. A careful experimental control is thus essential for synthesizing pure $La_{2/3}TiO_3$ [1]. The slightly oxygen-deficient $La_{2/3}TiO_{3-\lambda}$ with a non-negligible contribution of Ti^{3+} was prepared using conventional solid-state reaction in a reduced CO_2–H_2 atmosphere at 1,350 °C [19], using flux growth in air [20], and using hydrothermal method [21]. It was reported that a finite amount of Na^+, K^+, and/or Li^+ doping on the A-site is also favorable to stabilize the $La_{2/3}TiO_3$-type phase [12, 22]. Škapin et al. further indicated that firing stoichiometric $La_2O_3/3TiO_2$ at a temperature above the melting point of $La_4Ti_9O_{24}$ ~1455 °C in air results in the presence of Ti^{3+}, dramatically stabilizing the $La_{2/3}TiO_3$-type perovskite [2]. Other studies also pointed out that the $La_{2/3}TiO_3$-type phase

Y.-W. Liu · P. Lin (✉)
Department of Materials Science and Engineering, National Chiao Tung University, Hsinchu 300, Taiwan
e-mail: Panglin@cc.nctu.edu.tw

M.-W. Chu
Nanomaterials Laboratories, National Institute for Materials Science, 1-1 Namiki, Tsukuba, Ibaraki 305-0044, Japan

Fig. 1 (**a**) La$_4$Ti$_9$O$_{24}$ unit cell in [001] direction [3]. For simplicity, bonds and polyhedra are not shown. (**b**) The sandwiched region between two consecutive La(3)-centered polyhedra in [001] direction, showing TiO$_6$ network. (**c**) The same region as in (**b**) in [010] direction
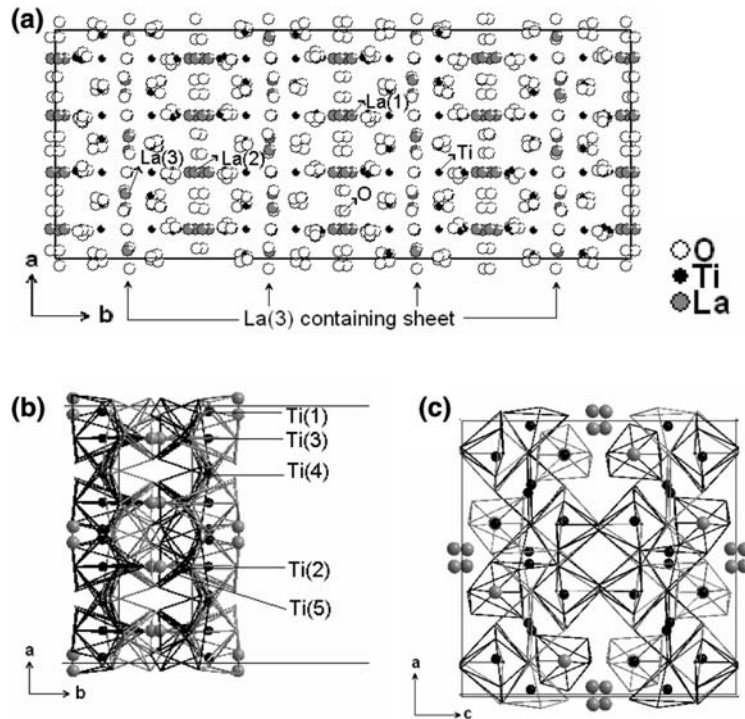
can co-exist with ferroelectric perovskites [14, 23–26] and LaNO$_3$ (N = Al^{3+}, Ga^{3+} and Fe^{3+}, Refs. [8, 13, 26–29]). More importantly, the crystal structure of the La$_{2/3}$TiO$_3$-type phase is characterized by a long-range cation/vacancy ordering on the perovskite A-site [7, 12, 22, 28, 29].

There have been numerous studies concerning influences of Pb^{2+} doping on the La$_2$O$_3$–TiO$_2$ system [30, 31], whereas a detailed report particularly on the Pb^{2+}–La$_4$Ti$_9$O$_{24}$ system remains lacking. We thus performed a systematic investigation of La$_4$Ti$_9$O$_{24}$ ceramics with various Pb^{2+} doping and further discussed the correlation with the La$_{2/3}$TiO$_3$-type phase.

Experiments

The La$_4$Ti$_9$O$_{24}$ compounds with various Pb^{2+}-doping degrees were prepared by the chemical co-precipitation method as shown in Fig. 2. La(NO$_3$)$_3$ · 6H$_2$O (Strem chemicals, (99.9%), TiCl$_4$ (Merck, (99%), Pb(NO$_3$)$_2$ (Showa chemical, 99.5%), and NH$_4$OH (TEDIA company, ACS grade) were exploited as the starting chemicals. The concentration of the mixture solution was kept at ~0.1 M for all syntheses with D.I. water as the solvent. The co-precipitated powders were then calcined at 900 °C for 1 h in air.

The La$_4$Ti$_9$O$_{24}$ ceramic bulks for performing Pb^{2+}/La$_4$Ti$_9$O$_{24}$ interaction investigations were prepared by conventional solid-state reaction. After mixing and calcination at 1,000 °C for 1 h in air, the powders were then ground,

sieved, and pressed into pellets (9 mm in diameter and 2 mm in thickness) for further sintering at 1,350 °C for 4 h in air. Subsequently, the sintered pellets were polished and coated
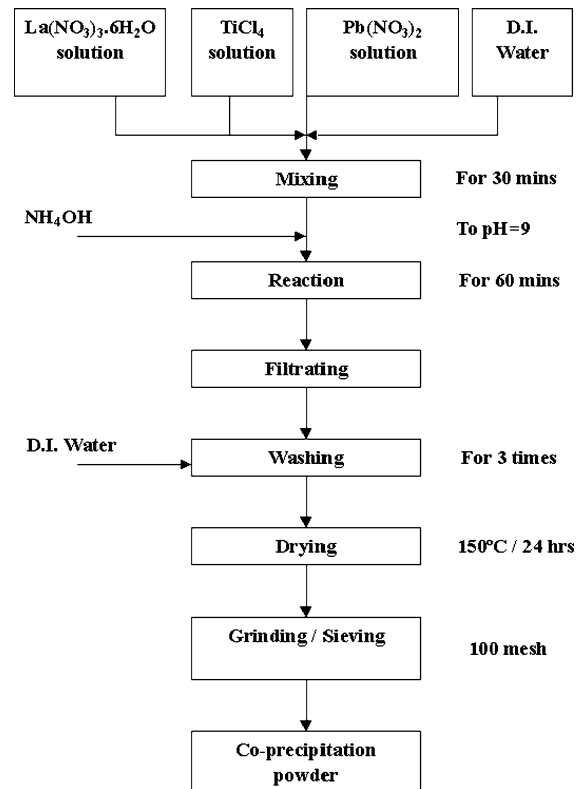
Fig. 2 Schematic co-precipitation preparation of La–Pb–Ti–O powders

with the PbO slurry, to prevent the PbO coated on the samples escaping when heating, the samples were put into closed platinum crucible with extra PbO powders around the samples. Followed by annealing at 750, 775, 800, 825, 850, 875, and 900 °C for 0.5–14 h using a pre-heated vertical furnace with an air-atmosphere quenching after the heat treatment. The cross-sectional $Pb^{2+}/La_4Ti_9O_{24}$ ceramic specimens was then polished and studied by SEM (HITACHI S2500) equipped with EDX and WDX.

The X-ray diffraction (XRD) patterns were recorded at room temperature using a MACScience M18XHF diffractometer with Cu-$K\alpha_1$ radiation. The transmission electron microscopy (TEM) study was performed on JEOL 2000FX operating at 200 kV.
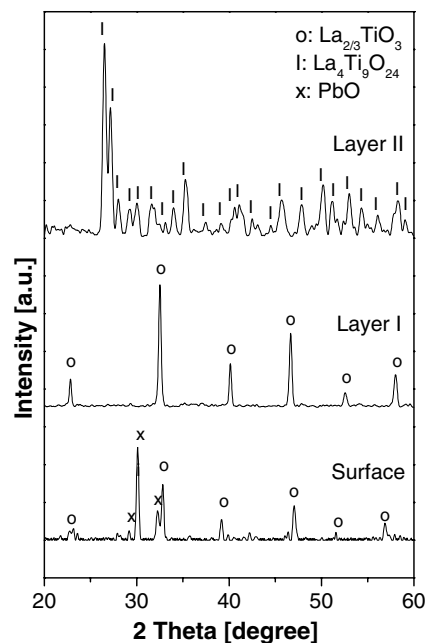
Results and discussion

The interaction between Pb^{2+} and sintered $La_4Ti_9O_{24}$

In order to understand the interaction between Pb^{2+} and $La_4Ti_9O_{24}$, the PbO coated ceramic bulk was annealed at 900 °C for 4 h. Figure 3 shows the SEM/EDS analysis of thus-prepared sample, revealing a significant Pb^{2+} diffusion into $La_4Ti_9O_{24}$. Further XRD studies were thus performed to investigate the crystallization of each layer indicated in Fig. 3. Figure 4 shows the corresponding XRD pattern and a significant crystallization of the $La_{2/3}TiO_3$-type phase is clearly observed in Layer I.

The Pb^{2+} diffusion into crystalline $La_4Ti_9O_{24}$ results in an increase in the internal stress of $La_4Ti_9O_{24}$ due to
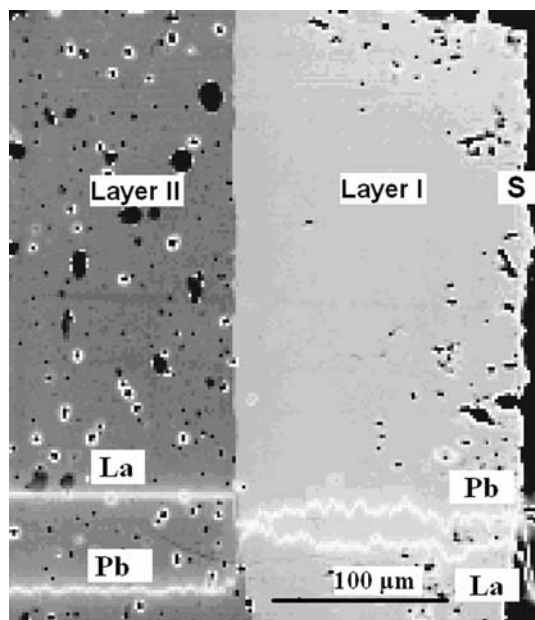
Fig. 4 The corresponding XRD patterns of the sample in Fig. 3

the relatively large size of Pb^{2+} ($r = 0.129$ nm, CN = 8) compared to La^{3+} ($r = 0.118$ nm, CN = 8) and the stereochemical activity of $6s^2$ lone-pair electrons of Pb^{2+} [32]. The formation of the corner-sheared TiO_6 configuration could be a feasible approach to relax this internal stress, thus leading to the modification of the $La_4Ti_9O_{24}$ lattice (see Fig. 1) further favoring the distorted $La_{2/3}TiO_3$-type perovskite [33]. In another view of the influence of impurities on the stability of $La_{2/3}TiO_3$ [12–15, 22–29], the $La_{2/3}TiO_3$-type perovskite structure could be stabilized by the partial filling of the A-site vacancies with Pb^{2+} ions.

The TEM micrograph of the cross-sectional Pb^{2+} diffused area /$La_4Ti_9O_{24}$ interface is shown in Fig. 5a, and the corresponding selected-area electron diffraction (SAED) pattern of the Pb^{2+} diffused area is depicted in Fig. 5b. The estimation of the real-space distance between the first intense ring and the transmitted beam leads to ~0.28 nm (see Fig. 5b), suggesting the possible crystallization of a perovskite-related phase at the interface with a_p ~0.38 nm (a_p, the prototypical lattice parameter of cubic perovskites) in consistency with the XRD study shown in Fig. 4. Further measuring the composition in the vicinity of the interface by WDX gives rise to $(La_{0.44}Pb_{0.34})TiO_3$ that is close to the intersection of the PbO–$La_4Ti_9O_{24}$ Alkemade line and the $PbTiO_3$–$La_{2/3}TiO_3$ tie line (see Fig. 6, the nominal composition of $(La_{0.44}Pb_{0.33})TiO_3$). Taking above characteristics into account, we thus proceeded to synthesize the $La_{2/3}TiO_3$-type phase by Pb^{2+}-doping into $La_4Ti_9O_{24}$.
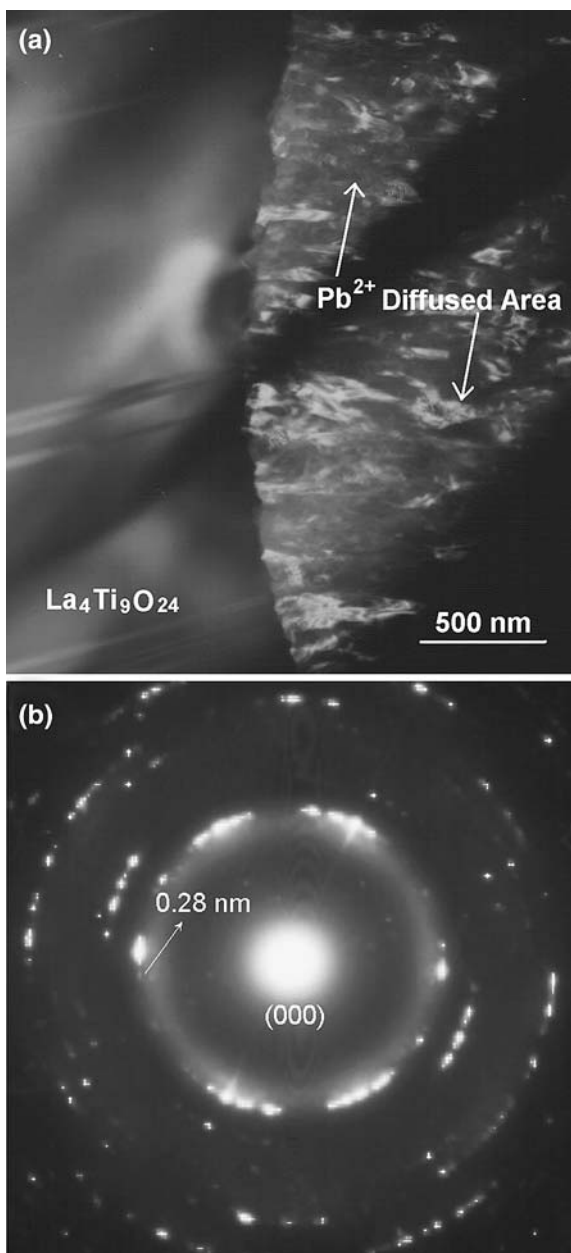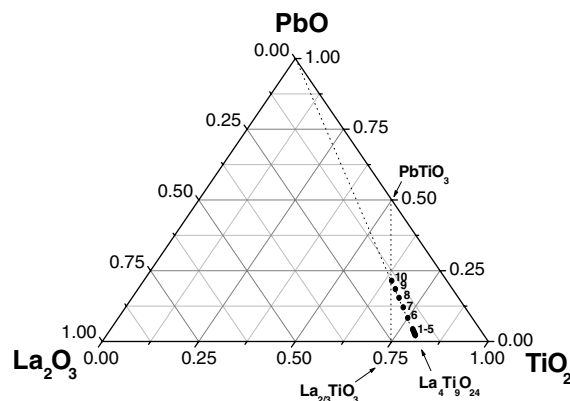

Fig. 3 SEM micrograph and EDX line scan of the cross-sectional $Pb^{2+}/La_4Ti_9O_{24}$ ceramics. **S** denotes the free surface

Fig. 5 (**a**) TEM image of the Pb^{2+} diffused area/$La_4Ti_9O_{24}$ interface and (**b**) the corresponding SAED pattern of the Pb^{2+} diffused area

Fig. 6 The equilibrium phase diagram of PbO–La_2O_3–TiO_2

Table 1 The nominal compositions of the co-precipitated powders

Specimen no.	Nominal composition	Composition (mole)		
		La^{3+}	Ti^{4+}	Pb^{2+}
1	$(La_{0.44}Pb_{0.03})TiO_{3-\delta}$	4.00	9.00	0.30
2	$(La_{0.44}Pb_{0.038})TiO_{3-\delta}$	4.00	9.00	0.35
3	$(La_{0.44}Pb_{0.044})TiO_{3-\delta}$	4.00	9.00	0.40
4	$(La_{0.44}Pb_{0.05})TiO_{3-\delta}$	4.00	9.00	0.45
5	$(La_{0.44}Pb_{0.06})TiO_{3-\delta}$	4.00	9.00	0.50
6	$(La_{0.44}Pb_{0.11})TiO_{3-\delta}$	4.00	9.00	1.00
7	$(La_{0.44}Pb_{0.17})TiO_{3-\delta}$	4.00	9.00	1.50
8	$(La_{0.44}Pb_{0.22})TiO_{3-\delta}$	4.00	9.00	2.00
9	$(La_{0.44}Pb_{0.28})TiO_{3-\delta}$	4.00	9.00	2.50
10	$(La_{0.44}Pb_{0.33})TiO_3$	4.00	9.00	3.00

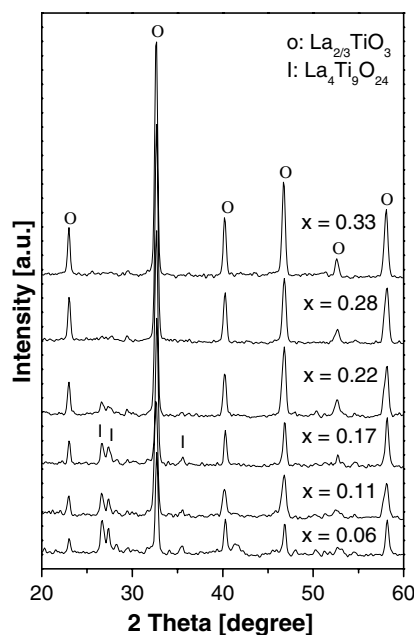### Study of co-precipitated Pb^{2+}-doped $La_4Ti_9O_{24}$

The nominal compositions exploited in the synthesis are given in Table 1, and the specimen indices are also shown in Fig. 6. Note that specimen No. 10 is the intersection composition of the PbO–$La_4Ti_9O_{24}$ Alkemade line and the $PbTiO_3$–$La_{2/3}TiO_3$ tie line. The XRD patterns of the co-precipitation powders calcined at 900 °C are shown in Fig. 7, revealing the increase in the $La_{2/3}TiO_3$-type phase with the increase in the Pb^{2+} doping. When the Pb^{2+} doping approaches 3 moles, the $La_{2/3}TiO_3$-type structure becomes the dominant phase.
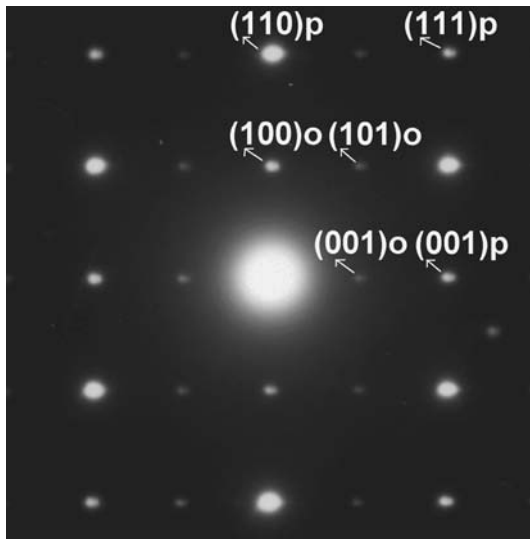

Fig. 7 XRD patterns of co-precipitated $(La_{0.44}Pb_x)TiO_3$ powders calcined at 900 °C for 1 h in air with different Pb^{2+} concentration

Fig. 8 The $[-110]_p$-zone SAED pattern of $(La_{0.44}Pb_{0.33})TiO_3$. The subscript 'o' represents the orthorhombic superstructure

The $[-110]_p$-zone SAED pattern of specimen No.10 is shown in Fig. 8 (the subscript 'p' denoting cubic perovskites). Note that this pattern shows extra weak reflections, $(001)_O$ and $(101)_O$, indicating an orthorhombic superlattice with $a \sim b \sim 0.55$ nm $\sim\sqrt{2}a_p$ and $c \sim 0.77$ nm $\sim 2a_p$. Furthermore, the indices of the weak reflections are compatible with the space group *Ibmm* (No. 74). In the study of $La_{1-x}TiO_3$ ($0 \le \times \le 0.33$) [7], it has been suggested that the crystal structure of the material is a function of the corresponding composition, *Pbnm* (No. 62, $0 \le \times \le 0.2$), *Ibmm* (No. 74, 0.2 ($\times \le 0.25$), and *Pban* (No. 50, 0.25 ($\times \le 0.33$). Moreover, the three orthorhombic cells all possess similar lattice parameters of $a \sim b \sim \sqrt{2}\ a_p$ and $c \sim 2a_p$. Considering the above features, specimen No. 10 with nominal $(La_{0.44}Pb_{0.33})TiO_3$ should thus exhibit the space group *Ibmm* (No. 74), which is indeed observed in the SAED study (see Fig. 8).

We then performed Rietveld analysis (RIETICA software [34]) on the XRD pattern of specimen No.10 using space group *Ibmm* (No. 74) with the nominal composition

Table 2 The Rietveld refinement results of $La_{0.44}Pb_{0.33}TiO_3$

	$La_{0.44}Pb_{0.33}TiO_3$
2 Theta range	20–80°
Step size	0.02°
Step time	0.5 s
Crystal class	Orthorhombic
Space group	*Ibmm* (No. 74)
A	0.55371 nm
B	0.55064 nm
C	0.77825 nm
V	0.23728 nm³
Calculated density	6.018 g/cm³

$(La_{0.44}Pb_{0.33})TiO_3$. The refined lattice parameters are shown in Table 2, and the presence of heavy Pb limits the determination of the respective atomic position with enough precisions [35].

Kinetic studies of Pb^{2+} diffusion into $La_4Ti_9O_{24}$

The kinetics of Pb^{2+} diffusion into $La_4Ti_9O_{24}$ ceramics was investigated at various annealing temperatures and the average thickness of the reacted layer was estimated by SEM. Figure 3 represents a typical example of the SEM estimation of the reacted layer. The reacted zone consists of the orthorhombic $La_{2/3}TiO_3$-type phase with the nominal composition $(La_{0.44}Pb_{0.33})TiO_3$. Figure 9 exhibits the linear dependence of the square of the thickness of the reacted layer, x, on the heat-treated time, t, in excellent agreement with the parabolic law $x^2 = kt$, where k is the growth rate coefficient. The kinetic study thus indicates that the Pb^{2+}/$La_4Ti_9O_{24}$ interaction strictly obeys the theory of the reactive diffusion [36, 37]. Calculating the gradient of each line in Fig. 9 leads to the growth rate coefficient, k, at different annealing temperatures, tabulated in Table 3. Furthermore, the experimental k values were used to determine the associated activation energy, E_a, for the formation of orthorhombic $(La_{0.44}Pb_{0.33})TiO_3$ using the Arrhenius plot (Fig. 10) and the following least-square equation,

$$\ln(k) = -E_a/RT + A,$$

where T is the annealing temperature; R is the universal gas constant, and A is a constant, resulting in $E_a \sim 607 \pm 60$ kJ/mol. Similar E_a value of Pb^{2+} diffusion could be compared in the study of Cherniak et al. [38].

The good correlation between the parabolic rate constant for Pb^{2+} and that for the activation energy provides
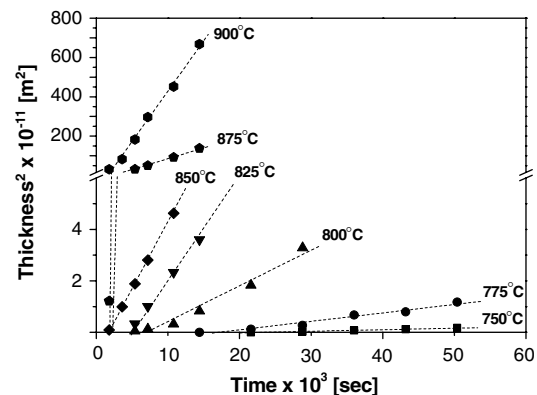
Fig. 9 The thickness square of the reacted layer at different temperatures as a function of on different annealing times

Table 3 The growth rate coefficient with different annealing temperatures

Temp. (°C)	750	775	800	825	850	875	900
k ($\times 10^{-15}$) [m^2 s^{-1}]	0.05	0.20	0.33	4.10	5.21	110.13	512.62
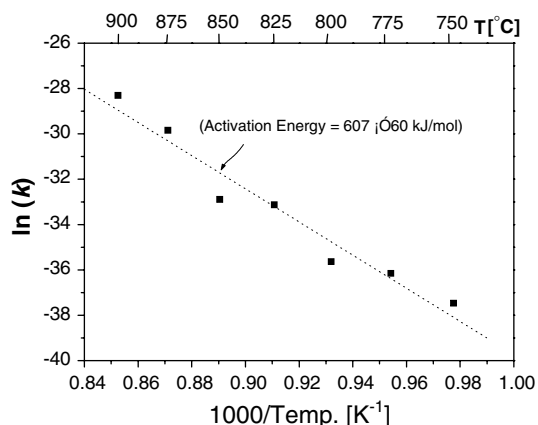
Fig. 10 Arrhenius plot of the growth rate coefficients

evidence to the assumption that the reaction kinetics of $(La_{0.44}Pb_{0.33})TiO_3$ phase formation is controlled by Pb^{2+} diffusion in the $(La_{0.44}Pb_{0.33})TiO_3$ ceramics, not the $Pb^{2+}/La_4Ti_9O_{24}$ interface reaction rate controlling process.

Conclusions

The structure of $La_4Ti_9O_{24}$ ceramics with different Pb^{2+} doping additions was investigated. When 1 mole of $La_4Ti_9O_{24}$ ceramics is reacted with 3 moles of PbO, the 'parent' $La_4Ti_9O_{24}$ phase transforms to the $La_{2/3}TiO_3$-type phase with a composition of $(La_{0.44}Pb_{0.33})TiO_3$. Further electron diffraction and XRD refinements indicated that $(La_{0.44}Pb_{0.33})TiO_3$ crystallizes in the orthorhombic space group *Ibmm* (No. 74) with $a = 0.55371$ nm, $b = 0.55064$ nm, and $c = 0.77825$ nm. The activation energy of this Pb^{2+}-induced phase transition is 607 ± 60 kJ/mol.

References

1. MacChesney JB, Sauer HA (1962) J Am Ceram Soc 45:416
2. Škapin S, Kolar D, Suvorov D (2000) J Eur Ceram Soc 20:1179
3. Morris RE, Owen JJ, Cheetham AK (1995) J Phys Chem Solids 56:1297
4. Takahashi J, Kageyama K, Kodaira K (1993) Jpn J Appl Phys 32:4327
5. Crandles DA, Timusk T, Garrett JD, Greedan JE (1994) Phys Rev B 49:16207
6. Park JK, Choi CH, Park HD, Choi SY (2001) J Mater Res 16:2568
7. MacEachern MJ, Dabkowska H, Garrett JD, Amow G, Gong W, Liu G, Greedan JE (1994) Chem Mater 6:2092
8. Yoshioka H, Kikkawa S (1998) J Mater Chem 8:1821
9. Jung WH (1999) J Mater Sci Lett 18:1181
10. Jung WH, Wakai H, Nakatsugawa H, Iguchi E (2000) J Appl Phys 85:2560
11. Yoshioka H (2002) J Am Ceram Soc 85:1339
12. Ruiz AI, López ML, Pico C, Veiga ML (2002) J Solid State Chem 163:472
13. Yoshioka H (1994) Jpn J Appl Phys 33:L945
14. Kim IS, Jung WH, Inaguma Y, Nakamura T, Itoh M (1995) Mat Res Bull 30:307
15. Suvorov D, Valant M, Škapin S, Kolar D (1998) J Mater Sci 33:85
16. Salak AN, Seabre MP, Ferreira VM (2003) J Eur Ceram Soc 23:2409
17. Liu YW, Lin P (2005) Mater Chem Phys 92:98
18. Liu YW, Lin P (2006) Mater Chem Phys (in press)
19. Abe M, Uchino K (1974) Mat Res Bull 9:147
20. Yokoyama M, Ota T, Yamai I, Takahashi J (1989) J Crystal Growth 96:490
21. Zheng W, Pang W (1997) Mater Lett 33:231
22. Ruiz AI, López ML, Veiga ML, Pico C (1999) J Solid State Chem 148:329
23. Sasaki H, Matsuo Y (1965) J Am Ceram Soc 48:434
24. Sasaki H, Matsuo Y (1972) Ceram Bull 51:164
25. Tien TY, Hummel FA (1967) Trans Brit Ceram Soc 66:233
26. Yoshioka H (1994) J Mater Res 9:2133
27. Škapin S, Kolar D, Suvorov D (1993) J Am Ceram Soc 76:2359
28. Hanžel D, Hanžel D, Meisel W, Kraševec V (1994) Hyperfine Interaction 92:1019
29. Lee HJ, Park HM, Cho YK (2003) J Am Ceram Soc 86:1395
30. Henning D (1971) Mat Res Bull 6:329
31. Prisedsky VV, Golubitsky VM (1992) Ferroelectrics 131:283
32. Goodenough JB, Longo JM (1978) In: Magnetic and other properties of oxides and related compounds. Landolt-Börnstein, New Series, Springer-Verlag, Berlin, 126 p
33. Mitchell RH (2002) In: Perovskites: modern and ancient. Almaz Press, Thunder Bay, Ontario, Canada
34. Hunter B (2000) LHPM-Rietica Rietveld. ANSTO, Australia
35. Noheda B, Cox DE, Shirane G, Gonzalo JA, Cross LE, Park S-E (1999) Appl Phys Lett 74:2059
36. Philibert J (1989) Defect Diffus Forum 66–69:995
37. Dybkov VI (1986) J Mater Sci 21:3078
38. Cherniak DJ, Watson EB, Grove M, Harrison TM (2004) Geochim Cosmochim Acta 68:829